

Experimental observation of the Yang-Lee quantum criticality in open systems

Huixia Gao,¹ Kunkun Wang,² Lei Xiao,^{3,1} Masaya Nakagawa,⁴ Norifumi Matsumoto,⁴ Dengke Qu,¹ Haiqing Lin,⁵ Masahito Ueda,^{4,6,7,*} and Peng Xue^{3,1,†}

¹*Beijing Computational Science Research Center, Beijing 100084, China*

²*School of Physics and Optoelectronic Engineering, Anhui University, Hefei 230601, China*

³*School of Physics, Southeast University, Nanjing 211189, China*

⁴*Department of Physics, University of Tokyo, 7-3-1 Hongo, Bunkyo-ku, Tokyo 113-0033, Japan*

⁵*School of Physics, Zhejiang University, Hangzhou 310030, China*

⁶*Institute for Physics of Intelligence, University of Tokyo, 7-3-1 Hongo, Bunkyo-ku, Tokyo 113-0033, Japan*

⁷*RIKEN Center for Emergent Matter Science (CEMS), Wako 351-0198, Japan*

The Yang-Lee edge singularity was originally studied from the standpoint of mathematical foundations of phase transitions, and its physical demonstration has been of active interest both theoretically and experimentally. However, the presence of an imaginary magnetic field in the Yang-Lee edge singularity has made it challenging to develop a direct observation of the anomalous scaling with negative scaling dimension associated with this critical phenomenon. We experimentally implement an imaginary magnetic field and demonstrate the Yang-Lee edge singularity through a nonunitary evolution governed by a non-Hermitian Hamiltonian in an open quantum system, where a classical system is mapped to a quantum system via the equivalent canonical partition function. In particular, we directly observe the partition function in our experiment using heralded single photons. The nonunitary quantum criticality is identified with the singularity at an exceptional point. We also demonstrate unconventional scaling laws for the finite-temperature dynamics unique to quantum systems.

Introduction.—Yang-Lee zeros [1, 2] are the zero points of the partition function appearing only on the complex plane of the physical parameters and provide key properties of phase transitions, such as critical exponents [3]. Yang and Lee [1, 2] showed that zeros of the partition function of the classical ferromagnetic Ising model are distributed on the imaginary axis of the complex magnetic field [4–6]. Yang-Lee zeros are also related to singularities [7–16] in thermodynamic quantities. When the distribution of Yang-Lee zeros pinches (crosses) the real axis, the system exhibits a second-order (first-order) phase transition. Furthermore, the distribution itself exhibits a singularity at its edges, and such singularity is called the Yang-Lee edge singularity, which stands as a prototypical instance of nonunitary critical phenomena exhibiting anomalous scaling laws unseen in unitary critical systems [17–20].

Due to their fundamental importance, Yang-Lee zeros and Yang-Lee edge singularity have been of theoretical [21–26] and experimental [27–35] interest. However, the presence of an imaginary magnetic field in the Yang-Lee edge singularity has made it challenging to develop a direct observation method and understand the physical implications of the anomalous scaling with negative scaling dimension associated with this phenomenon. Here the negative scaling dimension indicates that correlation functions diverge algebraically under space-time dilations and it is characteristic of nonunitary critical phenomena. A recent theoretical discovery demonstrates that the implementation of the Yang-Lee edge singularity in quantum systems is achievable through the utilization of the quantum-classical correspondence [36, 37]. This correspondence allows for the mapping of a classical system onto a quantum system by employing the equivalent canonical partition function [38].

In this Letter, we experimentally implement an imaginary magnetic field and demonstrate the Yang-

Lee edge singularity through a nonunitary evolution governed by a non-Hermitian Hamiltonian in an open quantum system. The Yang-Lee zeros and the Yang-Lee edge singularity of the classical ferromagnetic Ising model are both displayed in the quantum system due to the quantum-classical correspondence. The nonunitary quantum criticality is identified with the singularity at an exceptional point. We also show unconventional scaling laws for finite-temperature dynamics which are unique to quantum systems. Furthermore, we present the phase diagram of the Yang-Lee quantum critical system, where Yang-Lee zeros appear in the parity-time (\mathcal{PT})-broken phase. Our work is the first to measure all the critical exponents of the magnetization, magnetic susceptibility, two-time correlation function, and the density of zeros about the Yang-Lee edge singularity [39]. In particular, we directly observe the partition function, which gives a crucial advantage in the study of Yang-Lee zeros and related topics.

Yang-Lee edge singularity in open quantum systems.—We consider the Yang-Lee edge singularity in the classical one-dimensional Ising model with a pure-imaginary magnetic field $H = -J \sum_j \sigma_j \sigma_{j+1} - ih \sum_j \sigma_j$ [9], where $J > 0$, $h \in \mathbb{R}$, and $\sigma_j = \pm 1$. This model can be mapped to a quantum system governed by a \mathcal{PT} -symmetric non-Hermitian Hamiltonian via the quantum-classical correspondence [40, 41]

$$H_{\mathcal{PT}} = R \cos \phi \sigma_x + iR \sin \phi \sigma_z, \quad (1)$$

where $R > 0$, $\phi \in (-\pi/2, \pi/2)$, and σ_x and σ_z are the Pauli matrices. The canonical partition function of H is derived using the path-integral representation outlined in Eq. (1) for its quantum counterpart. On the basis of the partition functions' equivalence, Matsumoto *et al.* [38] pointed out that the latter quantum system exhibits a criticality equivalent to the Yang-Lee edge singularity in the former classical system.

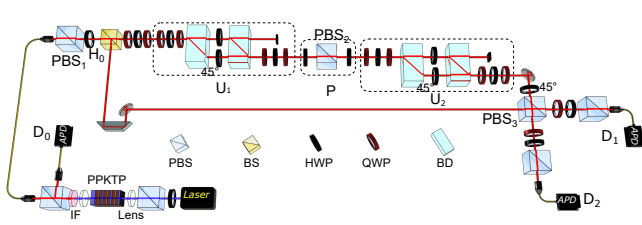


FIG. 1. Experimental setup. Heralded single photons are created via type-II spontaneous parametric down-conversion. The polarization beam splitter (PBS₁) and the half-wave plate (HWP) H_0 are used to generate initial polarization states $|H\rangle$ and $|V\rangle$. After photons pass through a 50 : 50 beam splitter (BS), the transmitted photons enter the evolution path, and the reflected photons act as reference photons and interfere with the transmitted photons at PBS₃. The evolution process is divided into four parts. The elimination of the global phase is realized by wave plates. The nonunitary evolutions U_1 and U_2 are realized by two beam displacers (BDs) and sets of wave plates. The projector P is realized by two HWPs and PBS₂. The measurement part is realized by PBS₃, two quarter-wave plates (QWPs) and two HWPs. Finally, photons are detected by avalanche photodiodes (APDs), and recording the coincidence counts of D_0 , D_1 and D_0 , D_2 , respectively.

The Hamiltonian $H_{\mathcal{PT}}$ satisfies the \mathcal{PT} symmetry with $[H, \mathcal{PT}] = 0$, where $\mathcal{P} = \sigma_x$, $\mathcal{T} = \mathcal{K}$, and \mathcal{K} is complex conjugation. The eigenenergies of the Hamiltonian are $E_{\pm} = \pm R\sqrt{\cos 2\phi}$. The exceptional points [42, 43] are located at $\phi = \pm\pi/4$, separating the \mathcal{PT} -unbroken and broken regimes.

The Yang-Lee edge singularity occurs at the edges of the distribution of zeros of the partition function

$$Z = \text{Tr} [e^{-\beta H_{\mathcal{PT}}}] = \sum_{p=\pm} e^{-\beta E_p}, \quad (2)$$

where β is the inverse temperature. The Yang-Lee quantum critical phenomena appear in the expectation value of a certain observable O given by [38, 44–47]

$$\langle O \rangle = \frac{\text{Tr} [O e^{-\beta H_{\mathcal{PT}}}]}{Z} = \frac{1}{Z} \sum_{p=\pm} \frac{\langle E_p^L | O | E_p^R \rangle}{\langle E_p^L | E_p^R \rangle} e^{-\beta E_p}, \quad (3)$$

where $|E_p^R\rangle$ ($\langle E_p^L|$) is the right (left) eigenvector of $H_{\mathcal{PT}}$. We simulate the \mathcal{PT} -symmetric nonunitary quantum dynamics using a single-photon interferometric network, and experimentally investigate the Yang-Lee quantum criticality.

Experimental demonstration.—To simulate the dynamics of the two-level \mathcal{PT} -symmetric system governed by $H_{\mathcal{PT}}$, we employ as the basis states the horizontal and vertical polarization states of a heralded single photon, i.e., $\{|0\rangle = |H\rangle, |1\rangle = |V\rangle\}$. Instead of implementing the non-Hermitian Hamiltonian $H_{\mathcal{PT}}$, we simulate the nonunitary quantum dynamics by directly implementing a nonunitary time-evolution operator U such that $U = e^{-iH_{\text{eff}}t}$ at any given time t (see Eq. (5)). Here the effective non-Hermitian Hamiltonian is given by

$$H_{\text{eff}} = H_{\mathcal{PT}} + \frac{d}{t} \mathbb{1}, \quad (4)$$

where $d = i \ln \frac{1}{\sqrt{\max |\lambda|}}$, λ is the eigenvalue of $e^{-iH_{\mathcal{PT}}t} e^{iH_{\mathcal{PT}}^\dagger t}$ [48, 49], and $\mathbb{1}$ is a 2×2 identity matrix. The probability amplitudes with respect to H_{eff} and $H_{\mathcal{PT}}$ are related to each other by $\langle j | e^{-iH_{\text{eff}}t} | j \rangle = \langle j | e^{-iH_{\mathcal{PT}}t} | j \rangle / \sqrt{\max |\lambda|}$, where $j = H, V$.

As illustrated in Fig. 1, the nonunitary operator U is implemented on the basis of the following decomposition:

$$U = R(\phi_2, \theta_2, \phi'_2) L(\theta_H, \theta_V) R(\phi_1, \theta_1, \phi'_1), \quad (5)$$

where the rotation $R(\phi_j, \theta_j, \phi'_j)$ ($j = 1, 2$) can be realized by a set of sandwiched wave plates with a configuration quarter-wave plate (QWP) at ϕ_j , a HWP at θ_j and a QWP at ϕ'_j , and the polarization-dependent loss operator L is realized by a combination of two beam displacers (BDs) and two HWPs with setting angles θ_H and θ_V . For each given evolution time t , the nonunitary evolution U can be realized by tuning the setting angles of wave plates [50] and mapped to $e^{-iH_{\mathcal{PT}}t}$ with a correction factor $\sqrt{\max |\lambda|}$.

We characterize scaling laws of physical quantities for a finite-temperature quantum system via the magnetization

$$m = \langle \sigma_z \rangle = \frac{\langle H | e^{-\beta H_{\mathcal{PT}}} | H \rangle - \langle V | e^{-\beta H_{\mathcal{PT}}} | V \rangle}{\langle H | e^{-\beta H_{\mathcal{PT}}} | H \rangle + \langle V | e^{-\beta H_{\mathcal{PT}}} | V \rangle}, \quad (6)$$

the magnetic susceptibility

$$\chi = \frac{dm}{da} = \frac{m - m'}{\tan \phi - \tan \phi'} \quad (7)$$

with $a = \tan \phi$ representing a normalized magnetic field and m (m') representing the magnetization for $H_{\mathcal{PT}}(\phi)$ ($H_{\mathcal{PT}}(\phi')$), and the two-time correlation function

$$G(t_2, t_1) = \langle \sigma_z(t_2) \sigma_z(t_1) \rangle - \langle \sigma_z(t_2) \rangle \langle \sigma_z(t_1) \rangle \quad (8)$$

$$= \frac{1}{Z} \left(\Sigma_{HH} \Sigma'_{HH} - \Sigma_{HV} \Sigma'_{VH} - \Sigma_{VH} \Sigma'_{HV} + \Sigma_{VV} \Sigma'_{VV} \right) - m^2,$$

where $\Sigma_{ij} = \langle i | e^{-i\Delta t H_{\mathcal{PT}}} | j \rangle$, $\Sigma'_{ij} = \langle i | e^{(i\Delta t - \beta) H_{\mathcal{PT}}} | j \rangle$ ($i, j = H, V$) and $Z = \langle H | e^{-\beta H_{\mathcal{PT}}} | H \rangle + \langle V | e^{-\beta H_{\mathcal{PT}}} | V \rangle$ is the partition function. Especially, the finite-temperature scaling of $G(t_2, t_1)$ is unique to quantum critical phenomena.

To measure the physical quantities experimentally, we use interference-based measurement. As illustrated in Fig. 1, after single photons pass through a beam splitter (BS), the transmitted photons as signal photons go through a nonunitary evolution, while the reflected photons as reference photons remain unchanged and then interfere with the transmitted ones after the evolution at a PBS. Via QWPs, HWPs and PBSs, projective measurements with the bases of $\{|+\rangle, |-\rangle, |R\rangle\}$ ($|\pm\rangle = (|H\rangle \pm |V\rangle)/\sqrt{2}$, $|R\rangle = (|H\rangle - i|V\rangle)/\sqrt{2}$) are then performed on the polarizations of the photons transmitted and reflected by the PBS. The outputs are recorded in coincidence with trigger photons. Typical measurements yield a maximum of 240,000 photon counts per second. For example, to measure m , we need

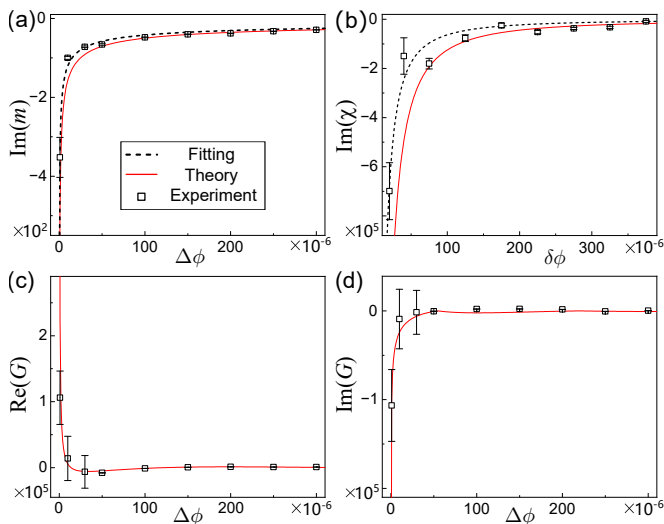


FIG. 2. Yang-Lee scaling laws of physical quantities for a finite-temperature quantum system in the \mathcal{PT} -unbroken phase in the limit $\phi \rightarrow \pi/4 - 0$ after $\beta^{-1} \rightarrow 0$. (a) The imaginary parts of m as a function of $\Delta\phi$. (b) The imaginary parts of χ as a function of $\delta\phi = (\Delta\phi + \Delta\phi')/2$, where $\Delta\phi = (10, 30, 50, 100, \dots, 350) \times 10^{-6}$ and $\Delta\phi' = (30, 50, 100, 150, \dots, 400) \times 10^{-6}$. Dependencies of real (c) and imaginary (d) parts of $G(t_2, t_1)$ on $\Delta\phi$. Experimental data are shown as open squares and theoretical predictions are represented by solid curves. We choose $R = 0.05$, $\beta = 10^5$ and $\Delta t = 3000$. Dashed curves in (a) and (b) correspond to the results fitted by different power laws. Error bars indicate the statistical uncertainty, which are obtained from Monte Carlo simulations under the assumption of Poissonian photon-counting statistics. Some error bars are smaller than the size of the symbols.

to obtain both $\langle H | e^{-\beta H_{\mathcal{PT}}} | H \rangle$ and $\langle V | e^{-\beta H_{\mathcal{PT}}} | V \rangle$. First, photons are prepared in the initial state $|H\rangle$ (or $|V\rangle$). After signal photons undergo a nonunitary evolution via $U = e^{-iH_{\text{eff}}t} = e^{-\beta H_{\mathcal{PT}}} / \sqrt{\max|\lambda|}$ (here we take $t = -i\beta$), they interfere with the reference photons in $|H\rangle$ (or $|V\rangle$) at the PBS. The inverse temperature β is taken as a parameter of the nonunitary evolution and tuned by the setting angles of wave plates. The overlap $\langle H(V) | e^{-\beta H_{\mathcal{PT}}} | H(V) \rangle$ can be calculated by the coincidence counts [39]. Similarly, we can obtain the overlaps $\Sigma_{ij}\Sigma'_{ji}$ in $G(t_2, t_1)$ by applying the nonunitary operations $U_1 = e^{-i\Delta t H_{\text{eff}}} = e^{-i\Delta t H_{\mathcal{PT}}} / \sqrt{\max|\lambda|}$ and $U_2 = e^{i(\Delta t - \beta)H_{\text{eff}}} = e^{i(\Delta t - \beta)H_{\mathcal{PT}}} / \sqrt{\max|\lambda|}$ and the projector $P = |j\rangle\langle j|$ on the signal photons.

Yang-Lee critical phenomena.—First, we discuss the scaling laws of the system in the \mathcal{PT} -unbroken phase ($|\phi| < \pi/4$) by examining the dependence of the physical quantities on the parameter $\Delta\phi := \pi/4 - \phi$. We consider two cases, in which we take either the limit $\phi \rightarrow \pi/4 - 0$ after $1/\beta \rightarrow 0$ or the limit $1/\beta \rightarrow 0$ after $\phi \rightarrow \pi/4 - 0$. Here $\beta^{-1} = 0$ corresponds to the thermodynamic limit of the classical one-dimensional Ising model, and the exceptional points $\phi = \pm\pi/4$ separate the \mathcal{PT} -unbroken and \mathcal{PT} -broken phases.

For the former case, the scaling laws are equivalent

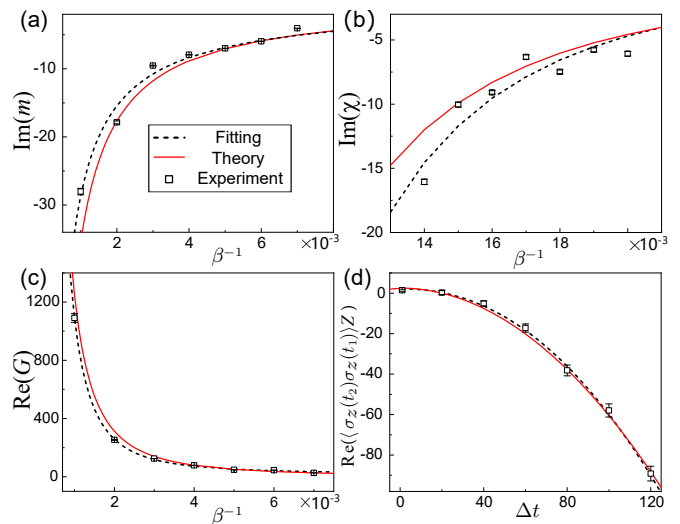


FIG. 3. Temperature dependences of anomalous scaling laws and Δt dependence of $\text{Re}(\langle \sigma_z(t_2) \sigma_z(t_1) \rangle Z)$ in the limit of $\beta^{-1} \rightarrow 0$ after $\phi \rightarrow \pi/4 - 0$. The imaginary parts of m (a) and χ (b) as functions of β^{-1} . (c) Real part of $G(t_2, t_1)$ as a function of β^{-1} . (d) Real part of $\langle \sigma_z(t_2) \sigma_z(t_1) \rangle Z$ as a function of Δt . We choose $R = 0.05$, $\phi = \pi/4 - 10^{-6}$ ($\phi' = \pi/4 - 10^{-2}$), $\Delta t = 0.1$ in (a), (b) and (c), and $R = 0.05$, $\phi = \pi/4 - 10^{-6}$, $\beta = 10^4$ in (d).

to those in the classical counterpart [9, 38], i.e.,

$$m \rightarrow \frac{-i \sin \phi}{\sqrt{\cos 2\phi}} \propto \Delta\phi^{-\frac{1}{2}}, \quad \chi \rightarrow \frac{-i \cos^3 \phi}{\cos^{\frac{3}{2}} 2\phi} \propto \Delta\phi^{-\frac{3}{2}},$$

$$G(t_2, t_1) \rightarrow \frac{\cos^2 \phi}{\cos 2\phi} \exp \left[-2\pi i \frac{\Delta t}{\pi / (R \sqrt{\cos 2\phi})} \right]. \quad (9)$$

We experimentally test these scaling laws for $R = 0.05$, $\beta = 10^5$, and various $\Delta\phi$. Since the real parts of m and χ are zeros, the scaling laws of them with respect to $\Delta\phi$ are characterized by their imaginary parts in Figs. 2(a) and (b), respectively. By fitting the power exponents to $m \sim \Delta\phi^r$, $\chi \sim \delta\phi^{r'}$, we obtain $r \sim -0.458 \pm 0.033$, $r' \sim -1.477 \pm 0.350$, which agree with their theoretical predictions -0.5 and -1.5 , respectively. The discrepancy with the theoretical predictions is mainly because the fitting result is sensitive to the difference between the leftmost experimental data point in Fig. 2(a) and its theoretical prediction, where the slope of the curve becomes large. In Figs. 2(c) and (d), we also show the measured values of $G(t_2, t_1)$ with respect to $\Delta\phi$ for $\Delta t = 3000$, which agree with the theoretical predictions [39].

For the latter case, we study the scaling laws

$$m \rightarrow -\frac{i}{\sqrt{2}}\beta R, \quad \chi \rightarrow -\frac{i}{3\sqrt{2}}(\beta^3 R^3 + \frac{3}{2}\beta R),$$

$$G(t_2, t_1) \rightarrow R^2 \left[\frac{1}{2}\beta^2 - i\beta\Delta t - (\Delta t)^2 \right] + 1, \quad (10)$$

which have not been discussed in the classical systems [9, 38]. The critical exponents for the power-law dependence on the temperature β^{-1} are -1 , -3 and -2 , respectively. In addition, the two-time correlation function scales as $G(t_2, t_1) \propto (\Delta t)^2$ in the limit of $\Delta t \rightarrow \infty$. If Δt is replaced by an imaginary-time interval $-i\Delta\beta$, $G(t_2, t_1)$ is equivalent to the spatial correla-

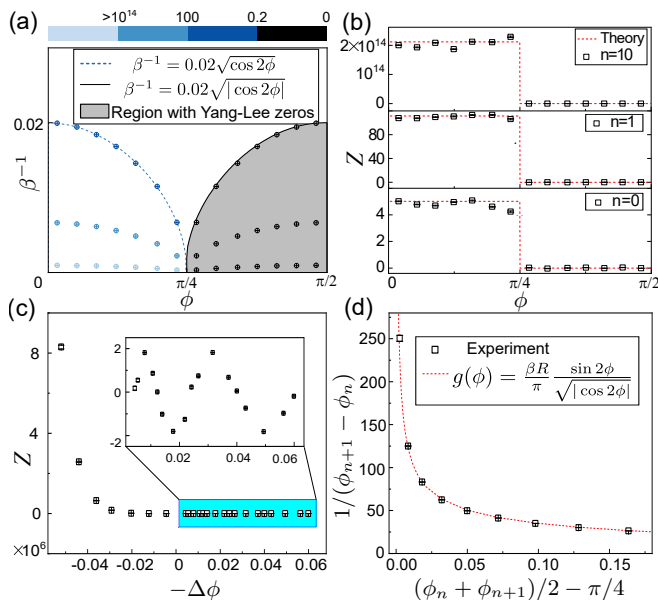


FIG. 4. (a) Phase diagram of the Yang-Lee quantum critical system. Experimental values of Z on the $\beta^{-1} - \phi$ plane. The critical point is located at $\phi = \pi/4$ and $\beta^{-1} = 0$. The Yang-Lee zeros appear in the \mathcal{PT} -broken ($\phi > \pi/4$) phase (the grey region) given by Eq. (13). In the \mathcal{PT} -unbroken phase, a crossover between Yang-Lee scaling laws and unconventional scaling laws occurs around the region indicated by the blue dashed curve. The experimental data are obtained with $n = 0, n = 1, n = 10$ from top to bottom, and the color indicates the value of Z . (b) Z as a function of ϕ with $n = 10, n = 1$ and $n = 0$, respectively. We choose $R = 0.01\pi$ for (a-b). For (c-d) we choose $R = 0.05$ and $\beta = 10^3$. (c) Z versus $-\Delta\phi$. The region colored in light blue shows the \mathcal{PT} -broken regime, and the inset is an enlarged view of the regime. (d) Density of zeros $1/(\phi_{n+1} - \phi_n)$ for $n = 0, 1, 2, \dots, 9$. The horizontal axis is taken as $(\phi_n + \phi_{n+1})/2$, which is measured from the critical point $\phi = \pi/4$.

tion function $G_{cl}(x)$ of the classical system with the distance $x = \Delta\beta$. The power-law scaling $G_{cl}(x) \propto x^{-2\Delta}$ with a negative scaling dimension $\Delta = -1$ is consistent with the critical scaling in the corresponding classical system [9]. To test this unconventional scaling laws, we choose $R = 0.05$, $\phi = \pi/4 - 10^{-6}$ ($\phi' = \pi/4 - 10^{-2}$), and $\Delta t = 0.1$. By fitting the power exponents with the formula $m \sim (\beta^{-1})^r$, $\chi \sim a(\beta^{-1})^{r'} + b(\beta^{-1})^r$, we obtain $r \sim -0.890 \pm 0.011$ and $r' \sim -3.171 \pm 0.062$, which agree with their theoretical predictions -1 and -3 , respectively. As illustrated in Fig. 3(c), by fitting the data with $G(t_2, t_1) \sim (\beta^{-1})^{r''}$, we obtain the experimental result $r'' \sim -2.160 \pm 0.021$, which is consistent with the theoretical critical exponent -2 .

We also show the Δt dependence of $\langle \sigma_z(t_2)\sigma_z(t_1) \rangle Z$ with $\beta = 10^4$ in Fig. 3(d), which is equivalent to the dependence of $G(t_2, t_1)$ because Z and m are independent of Δt [see Eq. (29)]. The power exponent is fitted by the formula $\langle \sigma_z(t_2)\sigma_z(t_1) \rangle Z \sim (\Delta t)^s$, and the obtained fitting result is $s \sim 2.187 \pm 0.089$, which is consistent with the theoretical prediction $G(t_2, t_1) \sim (\Delta t)^2$.

Phase diagram and partition function.—In the \mathcal{PT} -broken phase ($|\phi| > \pi/4$), m , χ and $G(t_2, t_1)$ diverge periodically in the limit $\phi \rightarrow \pi/4 + 0$ after $\beta^{-1} \rightarrow 0$ [38]. The corresponding experimental data can be found in

the Supplemental Material [39]. The condition for the divergence is

$$\beta R \sqrt{|\cos 2\phi|} = (n + \frac{1}{2})\pi, \quad (11)$$

where n is an integer, which corresponds to the condition for zeros of the partition function

$$Z = 2 \cos(\beta R \sqrt{|\cos 2\phi|}), \quad (12)$$

i.e., the Yang-Lee zeros. These zeros appear only in the region defined by

$$\beta^{-1} \leq \frac{2}{\pi} R \sqrt{|\cos 2\phi|}, \quad (13)$$

in the \mathcal{PT} -broken phase.

We measure the partition function Z on the $\beta^{-1} - \phi$ plane with $R = 0.01\pi$, $n = 0, n = 1$ and $n = 10$ in Eq. (16) for 14 different ϕ . As illustrated in Fig. 4(a), the Yang-Lee zeros appear only in the region given by Eq. (13) in the \mathcal{PT} -broken phase, which agrees with the theoretical prediction. As shown in Fig. 4(b), Z takes large positive values in the \mathcal{PT} -unbroken phase and drops in the \mathcal{PT} -broken phase. As illustrated in Fig. 4(c), we can see Z oscillating with $-\Delta\phi$ in the \mathcal{PT} -broken phase. Since the nodes of the oscillations correspond to Yang-Lee zeros, the period of the oscillation reflects the distance between Yang-Lee zeros. We can utilize Eq. (16) to understand the relationship between the period of the oscillation and the parameters β and R . For $R = 0.05$ and $\beta = 10^3$, we expect the oscillation period of ϕ to be $\pi/100$, which is consistent with the observed value of 0.03 . Thus, we observe the Yang-Lee zeros experimentally and also demonstrate that the Yang-Lee edge singularity indeed manifests itself as the distribution of zeros of Z .

Density of zeros.—For the $(0+1)$ -dimensional quantum Yang-Lee model in Eq. (1), the zero points $\{\phi_n\}_n$ of Z are determined from the condition in Eq. (16). The distribution of zeros of Z becomes dense if the limit $\beta R \rightarrow \infty$ is taken. We then calculate the density of zeros $g(\phi) := \sum_n \delta(\phi - \phi_n)$ and find a power-law behaviour

$$g(\phi) \propto (-\Delta\phi)^{-\frac{1}{2}} \quad (14)$$

near the critical point $\phi = \pi/4$. This result is consistent with the classical Yang-Lee edge singularity [3, 9]. In Fig. 4(d), we show the experimental results of the density of zeros $1/(\phi_{n+1} - \phi_n)$ for $n = 0, 1, 2, \dots, 9$, with the parameters $R = 0.05$ and $\beta = 10^3$. The horizontal axis is taken as $(\phi_n + \phi_{n+1})/2$, which is measured from the critical point $\phi = \pi/4$. Our experimental results agree well with the analytic expression of $g(\phi) = \frac{\beta R}{\pi} \frac{\sin 2\phi}{\sqrt{|\cos 2\phi|}}$ [39]. Via the density distribution of zeros experimentally observed for 10 different n 's, we have achieved the direct observation of the Yang-Lee edge singularity.

Conclusion.—The Yang-Lee edge singularity is a quintessential nonunitary critical phenomenon characterized by anomalous scaling. In this Letter, we have experimentally demonstrated the Yang-Lee singularity

in a non-Hermitian quantum system with \mathcal{PT} symmetry. Specifically, we have observed both anomalous scaling laws that are consistent with the classical Yang-Lee singularity and unconventional scaling laws that have not been discussed in classical systems. In particular, we directly observe the partition function in our experiment, which gives a decisive advantage in the study of Yang-Lee zeros and related topics. Our work presents the first experimental demonstration of the Yang-Lee quantum criticality in open quantum systems. We expect that the nonunitary critical phenomena in open quantum systems for higher-dimensional systems can also be probed using a similar approach.

Appendix A: Density of zeros in the $(0+1)$ -dimensional quantum Yang-Lee model

We consider the $(0+1)$ -dimensional quantum Yang-Lee model [38]

$$H_{\mathcal{PT}} = R \cos \phi \sigma_x + iR \sin \phi \sigma_z, \quad (15)$$

where $R > 0$, $\phi \in (-\pi/2, \pi/2)$, and σ_x and σ_z are the Pauli matrices. The partition function of this system in the \mathcal{PT} -broken regime ($|\phi| > \pi/4$) is given by $Z = \text{Tr}[e^{-\beta H_{\mathcal{PT}}}] = 2 \cos(\beta R \sqrt{|\cos 2\phi|})$. The zero points $\{\phi_n\}_n$ of the partition function are determined from the condition

$$\beta R \sqrt{|\cos 2\phi_n|} = (n + \frac{1}{2})\pi, \quad (16)$$

where $n = 0, 1, 2, \dots$.

The distribution of zeros of the partition function becomes dense if we take the limit $\beta R \rightarrow \infty$. The Yang-Lee edge singularity manifests itself as a power-law behavior of the density of zeros near the edge of the distribution [3, 7]. Here we calculate the density of zeros

$$g(\phi) := \sum_n \delta(\phi - \phi_n) \quad (17)$$

near the critical point $\phi = \pi/4$. To this end, we assume $\beta R \gg 1$ and introduce a continuous variable x that satisfies

$$x := \frac{\pi}{\beta R} n. \quad (18)$$

From Eq. (16), the zero points $\phi(x)$ satisfy

$$\cos 2\phi(x) = -(x + \frac{\pi}{2\beta R})^2 \quad (19)$$

and thus we have

$$\frac{dx}{d\phi} = \frac{\sin 2\phi}{x + \pi/(2\beta R)} = \frac{\sin 2\phi}{\sqrt{|\cos 2\phi|}}. \quad (20)$$

Then, the density of zeros can be calculated as

$$\begin{aligned} g(\phi') &:= \sum_n \delta(\phi' - \phi_n) \simeq \frac{\beta R}{\pi} \int dx \delta(\phi' - \phi(x)) \quad (21) \\ &= \frac{\beta R}{\pi} \int d\phi \frac{dx}{d\phi} \delta(\phi' - \phi) = \frac{\beta R}{\pi} \frac{\sin 2\phi'}{\sqrt{|\cos 2\phi'|}}. \end{aligned}$$

Thus, the density of zeros shows a power-law behavior near the critical point as

$$g(\phi) \propto (-\Delta\phi)^\sigma, \quad (22)$$

where $\Delta\phi := \pi/4 - \phi$ and $\sigma = -1/2$. The critical exponent $\sigma = -1/2$ agrees with the result for the classical one-dimensional Ising model [3, 9].

Appendix B: Measurement of the density of zeros in the Yang-Lee quantum criticality

To observe the power-law behaviour in the density of zeros, we choose the parameters $R = 0.05$ and $\beta = 10^3$ and show the experimental results of the density of zeros $1/(\phi_{n+1} - \phi_n)$ from $n = 0$ to 9 versus $(\phi_n + \phi_{n+1})/2 - \pi/4$. First, we choose several ϕ and measure the partition function Z experimentally. By fitting with $Z \sim \cos(\beta R \sqrt{|\cos 2\phi|})$, we obtain the experimental result $\beta R \sim 49.682 \pm 0.029$, which is consistent with the theoretical prediction of 50. Second, for $n = 0, \dots, 9$, we calculate ϕ_n from Eq. (11) of the main text and measure the corresponding partition function Z_n . With the measured Z_n and βR , we obtain the experimental results of ϕ_n from

$$\phi_n = \frac{1}{2} \arccos \left[- \left(\frac{1}{\beta R} \arccos \left(\frac{Z_n}{2} \right) \right)^2 \right]. \quad (23)$$

The experimental results of the density of zeros $1/(\phi_{n+1} - \phi_n)$ from $n = 0$ to 9 are shown in Fig. 4(d) of the main text. The horizontal axis is taken as $(\phi_n + \phi_{n+1})/2$, which is measured from the critical point $\phi = \pi/4$. Our experimental results agree well with the analytic expression Eq. (21). The Yang-Lee edge singularity manifests itself as the distribution of zeros for 10 different n 's.

Appendix C: Experimental implementation

Here we provide the method for measuring the physical quantities including the magnetization, the magnetic susceptibility, the two-time correlation function and the partition function. As demonstrated in the main text, these physical quantities can be obtained by measuring the probabilistic amplitudes of the final states.

For example, if we want to obtain the term $\langle 0 | e^{-\beta H_{\mathcal{PT}}} | 0 \rangle$ of the magnetization in Eq. (6) of the main text, we measure the probability amplitude p_1 which is related to the overlap between the initial state $|0\rangle$ and the final state after the nonunitary evolution $e^{-\beta H_{\mathcal{PT}}}$ as $\langle 0 | e^{-\beta H_{\mathcal{PT}}} | 0 \rangle = p_1 \times \sqrt{\max|\lambda|}$, where λ is the eigenvalue of $e^{-\beta H_{\mathcal{PT}}} e^{-\beta H_{\mathcal{PT}}^\dagger}$. Once we obtain the probability amplitude p_1 , we can calculate the measured overlap and the measured physical quantities.

Figure 5 shows the flow chart of state evolution and the schematic diagram of state evolving elements. In our experiment, a polarizing beam splitter (PBS) and a half-wave plate (HWP) H_0 realize the preparation

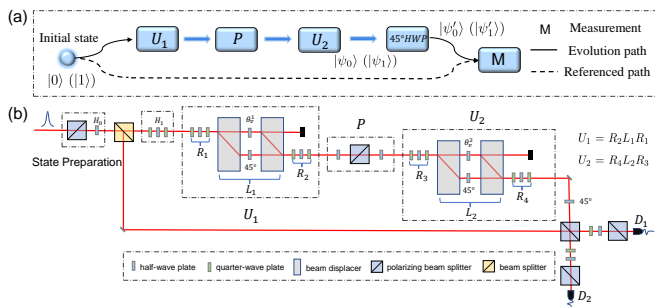


FIG. 5. Schematic diagrams of the experiment. (a) The flow chart of state evolution. Single photons with the initial state $|0\rangle$ or $|1\rangle$ goes through two paths of state evolution and reference. On the evolution path, single photons evolves into $|\psi_0\rangle$ or $|\psi_1\rangle$ after undergoing non-unitary evolutions U_1 , P , and U_2 , and then evolves into $|\psi'_0\rangle$ or $|\psi'_1\rangle$ by passing through a half-wave plate (HWP) at 45° . The photons remain unchanged on the reference path. Finally, we make measurements on the photons after they interfere. (b) Experimental setup which is the same as Fig. 1 in the main text.

of the initial state $|0\rangle$ or $|1\rangle$. After the heralded single photons pass through the 50 : 50 beam splitter (BS), the transmitted photons go through the nonunitary evolution and the reflected photons remain unchanged. The state of the transmitted photons then evolves according to $|\psi_0\rangle = e^{-\beta H_P \tau} |0\rangle = \begin{pmatrix} a_0 \\ b_0 \end{pmatrix}$ or $|\psi_1\rangle = e^{-\beta H_P \tau} |1\rangle = \begin{pmatrix} a_1 \\ b_1 \end{pmatrix}$. In the nonunitary evolution process, the elimination of the global phase is made by a HWP H_1 sandwiched between two quarter-wave plates (QWPs at 45°). To realize nonunitary evolution U_1 , we perform the singular value decomposition on the nonunitary matrix $U_1 = R_2 L_1 R_1$ [51]. The rotations R_1 and R_2 can be realized by a sandwich-type set of wave plates including a HWP and two QWPs. The loss operator $L_1 = \begin{pmatrix} 0 & \sin 2\theta_v^1 \\ 1 & 0 \end{pmatrix}$ is implemented by two HWPs at 45° and θ_v^1 , respectively, and two beam displacers (BDs). Similarly, we can realize another nonunitary evolution U_2 with the same method. For the projector P , $|0\rangle\langle 0|$ can be realized by a PBS, while $|1\rangle\langle 1|$ can be realized by a PBS and two HWPs at 45° . A HWP at 45° is applied to the polarizations of the transmitted photons. Then the state evolves into $|\psi'_0\rangle = \begin{pmatrix} b_0 \\ a_0 \end{pmatrix}$ or $|\psi'_1\rangle = \begin{pmatrix} b_1 \\ a_1 \end{pmatrix}$. The reflected photons act as reference photons and interfere with transmitted photons at the third PBS.

We perform projective measurements [52, 53] in the basis $\{|+\rangle, |-\rangle, |R\rangle\}$ on the polarizations of the photons in either of the transmitted (t) or reflected mode (r) of the third PBS. We denote the coincidence counts of D_0 and D_1 (D_0 and D_2) as N^r (N^t) when the initial state is $|0\rangle$ ($|1\rangle$), and the measured coincidence counts are denoted as $\{N_+^r, N_-^r, N_R^r\}$ ($\{N_+^t, N_-^t, N_R^t\}$), which

satisfy the following relations

$$\begin{aligned} N_+^r &= \mathcal{N} \frac{a_0^2 + 1 + a_0^* + a_0}{2}, & N_-^r &= \mathcal{N} \frac{a_0^2 + 1 - a_0^* - a_0}{2}, \\ N_R^r &= \mathcal{N} \frac{a_0^2 + 1 + i(a_0 - a_0^*)}{2}, & N_+^t &= \mathcal{N} \frac{b_1^2 + 1 + b_1^* + b_1}{2}, \\ N_-^t &= \mathcal{N} \frac{b_1^2 + 1 - b_1^* - b_1}{2}, & N_R^t &= \mathcal{N} \frac{b_1^2 + 1 + i(b_1^* - b_1)}{2}, \end{aligned} \quad (24)$$

where \mathcal{N} is the number of reference photons. We can obtain the probability amplitudes a_0 and b_0 through the following relations:

$$\begin{aligned} \text{Re}(a_0) &= \frac{N_+^r - N_-^r}{2\mathcal{N}}, & \text{Im}(a_0) &= \frac{1}{\mathcal{N}} \times \frac{N_+^r + N_-^r - 2N_R^r}{2}, \\ \text{Re}(b_1) &= \frac{N_+^t - N_-^t}{2\mathcal{N}}, & \text{Im}(b_1) &= \frac{1}{\mathcal{N}} \times \frac{2N_R^t - (N_+^t + N_-^t)}{2}. \end{aligned} \quad (25)$$

Then, we can calculate the measured overlap and the measured physical quantities from the real and imaginary parts of the amplitudes of the evolved states.

Appendix D: Additional experimental results

In this section, we present the additional part of the complex expectation values of observables presented in the main text.

The first task of our experiment in the main text is to find the imaginary parts of expectation values of the magnetization and the magnetic susceptibility for different values of ϕ [see Figs. 2(a) and (b) in the main text]. As shown in Figs. 6(a) and (b), the real parts of their expectation values are zero. In addition, we show the real and imaginary parts of the two-time correlation function for $\Delta\phi = \pi/4 - \phi$ with $\Delta t = 4000$, $\Delta t = 5000$, $\Delta t = 0.1$ and $\Delta t = 10$ in Figs. 6(c), (d), (e), (f), (g), (h), and (i), (j), respectively. It can be seen that the measured two-time correlation functions are consistent with their theoretical predictions for different time differences Δt .

The second task of our experiment in the main text is to find the imaginary parts of expectation values of the magnetization and the magnetic susceptibility for different values of β^{-1} [see Figs. 3(a) and (b) in the main text]. As shown in Figs. 7(a) and (b), the real parts of their expectation values are zero. In addition, for the expectation value of the two-time correlation function, we plot the imaginary parts against β^{-1} and Δt in Figs. 7(c) and (d), respectively. It can be seen that the measured two-time correlation functions are consistent with their theoretical predictions.

Here we comment on the choice of the parameters. In this work, we investigate two types of scaling laws, i.e., the Yang-Lee scaling laws [Eq. (9) in the main text] and the anomalous scaling laws [Eq. (10) in the main text]. Since the two scaling behaviors are separated by a crossover line $\beta^{-1} = (2R/\pi)\sqrt{\cos 2\phi}$ (see the phase diagram in Fig. 4(a) in the main text and Fig. 1 in Ref. [38]), the former should be observed if $\beta^{-1} \ll (2R/\pi)\sqrt{\cos 2\phi}$ and $\phi < \pi/4$, while the latter should

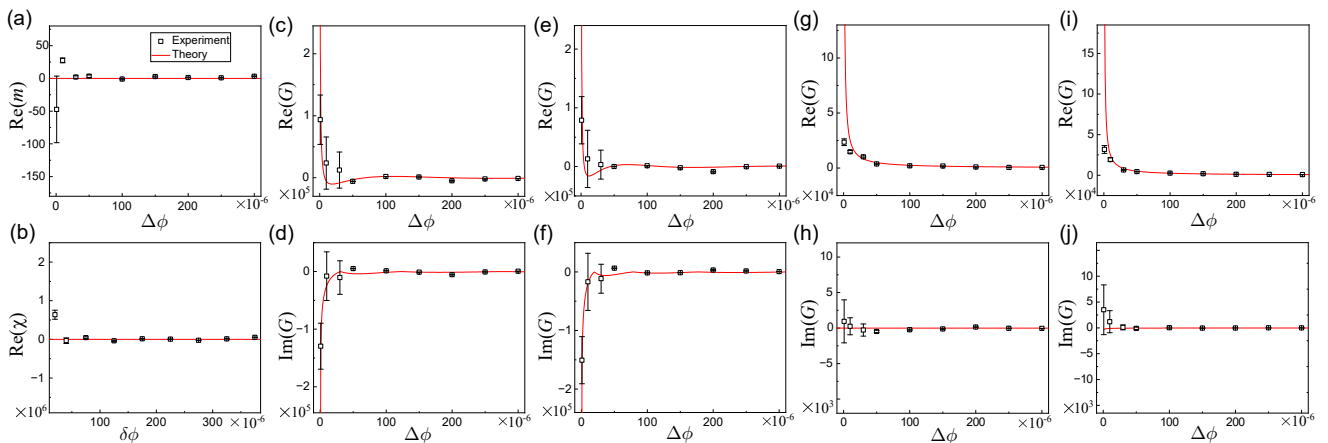


FIG. 6. (a) Real parts of the expectation value of the magnetization plotted against $\Delta\phi$. (b) Real parts of the expectation value of the magnetic susceptibility as a function of $\delta\phi = (\Delta\phi + \Delta\phi')/2$, where $\Delta\phi = 10 \times 10^{-6}, 30 \times 10^{-6}, 50 \times 10^{-6}, 100 \times 10^{-6}, \dots, 350 \times 10^{-6}$ and $\Delta\phi' = 30 \times 10^{-6}, 50 \times 10^{-6}, 100 \times 10^{-6}, 150 \times 10^{-6}, \dots, 400 \times 10^{-6}$. Real (c) and imaginary (d) parts of expectation values of the two-time correlation function for different $\Delta\phi$ with $\Delta t = 4000$. Real (e) and imaginary (f) parts of expectation values of the two-time correlation function plotted against $\Delta\phi$ with $\Delta t = 5000$. Real (g) and imaginary (h) parts of expectation values of the two-time correlation function plotted against $\Delta\phi$ with $\Delta t = 0.1$. Real (i) and imaginary (j) parts of expectation values of the two-time correlation function plotted against $\Delta\phi$ with $\Delta t = 10$. We choose $R = 0.05$ and $\beta = 10^5$. Black open squares indicate experimental data and red solid curves show theoretical predictions.

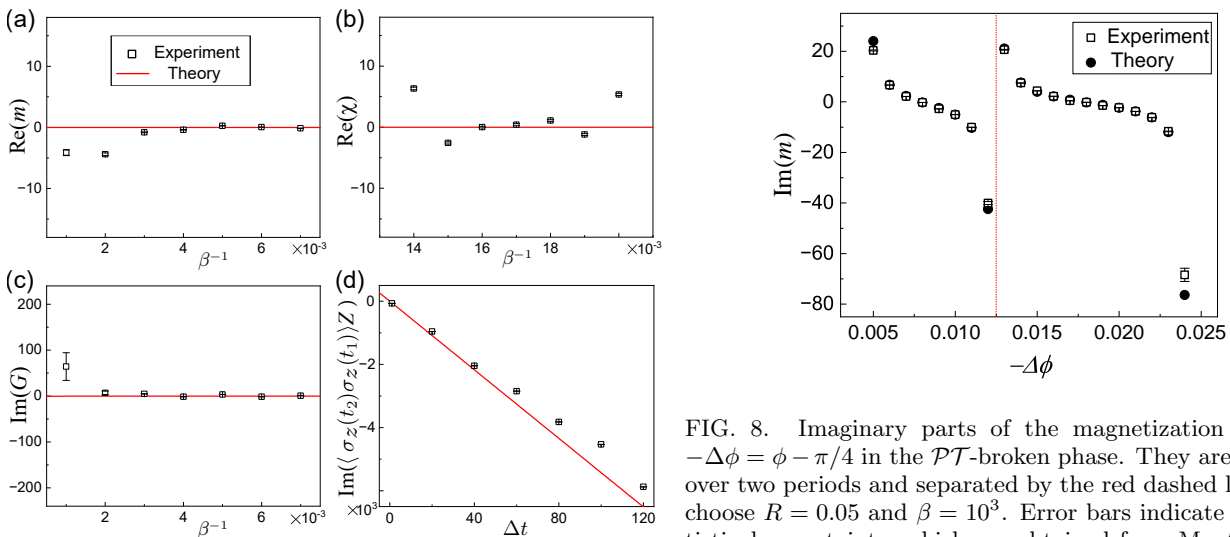


FIG. 7. (a) Real parts of the expectation value of the magnetization plotted against β^{-1} . (b) Real parts of the expectation value of the magnetic susceptibility plotted against β^{-1} . (c) Imaginary parts of expectation values of the two-time correlation function plotted against β^{-1} . (d) Imaginary parts of expectation values of $\langle \sigma_z(t_2)\sigma_z(t_1) \rangle / Z$ plotted against Δt . We choose $R = 0.05$, $\phi = \pi/4 - 10^{-6}$ ($\phi' = \pi/4 - 10^{-2}$), $\Delta t = 0.1$ in (a), (b) and (c), and $R = 0.05$, $\phi = \pi/4 - 10^{-6}$, $\beta = 10^4$ in (d). Black open squares indicate experimental data and red solid curves show theoretical predictions.

be observed if $(2R/\pi)\sqrt{|\cos 2\phi|} < \beta^{-1} \ll 2R/\pi$. The parameters in Figs. 2 and 3 are chosen so that these conditions are satisfied. In particular, in Fig. 3, we are concerned with the anomalous scaling behavior which becomes prominent at low temperatures. Therefore, if we make the value of $\pi/4 - \phi$ fixed to be a smaller one to examine the regime of smaller values of β^{-1} , we expect to obtain the critical exponents closer to the

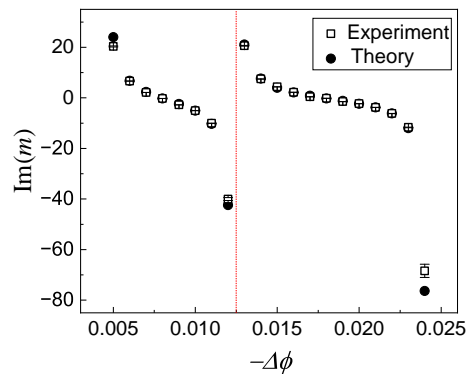


FIG. 8. Imaginary parts of the magnetization against $-\Delta\phi = \phi - \pi/4$ in the \mathcal{PT} -broken phase. They are plotted over two periods and separated by the red dashed line. We choose $R = 0.05$ and $\beta = 10^3$. Error bars indicate the statistical uncertainty, which are obtained from Monte Carlo simulations under the assumption of Poissonian photon-counting statistics. Some error bars are smaller than the size of the symbols.

theoretical predictions. Furthermore, the β^{-1} dependence of the two-time correlation function in Fig. 3(c) is expected to exhibit values of critical exponents closer to the theoretical predictions in the regime $\beta \gg \Delta t$.

In the \mathcal{PT} -broken phase, we experimentally confirm that the expectation value of the magnetization is pure imaginary for several different values of $\Delta\phi$. The third task shows imaginary parts of the expectation value of the magnetization in the \mathcal{PT} -broken phase in Fig. 8. We examine the dependence of the magnetization on ϕ by taking the limit $\phi \rightarrow \pi/4 + 0$ after $\beta^{-1} \rightarrow 0$. We examine the magnetization as an example for $R = 0.05$, $\beta = 10^3$, and 20 different values of ϕ . Since the real parts of the magnetization is zero, we only show its imaginary parts in two variation periods in Fig. 8. The magnetization exhibits a discontinuity with respect to

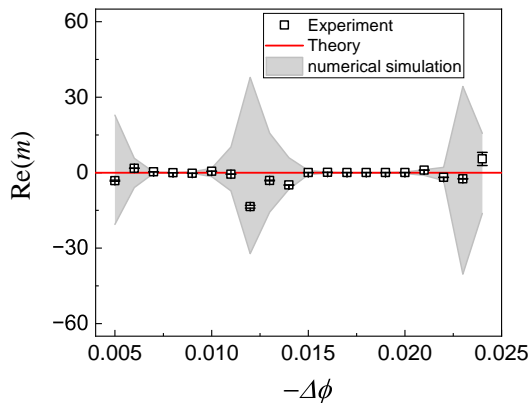


FIG. 9. Real part of the expectation value of the magnetization plotted against $-\Delta\phi$. We choose $R = 0.05$, $\beta = 10^3$. Open squares indicate experimental data, the solid line shows the theoretical prediction. Error bars indicate the statistical uncertainty, which are obtained from Monte Carlo simulations under the assumption of Poissonian photon-counting statistics. Some error bars are smaller than the size of the symbols. Shadows indicate systematic errors which are obtained from the numerical simulation by considering the inaccuracy of wave plates and decoherence in the experiment.

$-\Delta\phi$. The experimental results demonstrate that there is no scaling laws for the magnetization in the \mathcal{PT} -broken phase.

We show in Fig. 9 the real part of the expectation value of the magnetization for several different values of $-\Delta\phi$. The measured data are consistent with the theoretical predictions except for a few points that deviate from zero presumably due to systematic errors.

Appendix E: Error analysis

Two factors are responsible for the deviation between the experimental results and their theoretical predictions. On one hand, the imperfection of the experiment affects the results of the experiment. On the other hand, the value of the correction factor $\sqrt{\max|\lambda|}$ amplifies the imperfection of the experiment.

There are three major sources of imperfections in our experiment: photon fluctuations, inaccuracy of wave plates and decoherence (dephasing) caused by the imperfect interferometers. First, the imperfection caused by photon-number fluctuations decreases with increasing photon counts. In our experiment, the coincidence count per second is about 240,000, and the coincidence window is 150s. It can be seen from the data plots that the error bars caused by photon number fluctuations in our experiments are small. Second, for each wave plate, we assume an uncertainty in the setting angle $\theta + \delta\theta$. Here $\delta\theta$ is randomly chosen from the interval $[-1^\circ, 1^\circ]$ (normal accuracy range of wave plates). Third, the dephasing due to the imperfection of interferometric network with PBSs (BDs) affects the experimental results through a noisy channel $\varepsilon(\rho) = \eta\rho + (1-\eta)\sigma_z\rho\sigma_z$ ($\varepsilon(\rho) = \eta_1\rho + (1-\eta_1)\sigma_z\rho\sigma_z$) acting on the polarization state in different output modes. Here ρ ($\varepsilon(\rho)$) is the density matrix of the input (output) state of

TABLE I. The squared correction factor $\max|\lambda|$. The squared correction factor $\max|\lambda_Z|$ needs to be multiplied when measuring the partition function Z . The squared correction factor $\max|\lambda_G|$ needs to be multiplied when measuring $\langle\sigma_z(t_2)\sigma_z(t_1)\rangle Z$ to obtain the two-time correlation function $G(t_2, t_1)$.

(a) The squared correction factors $\max|\lambda_Z|$ and $\max|\lambda_G|$ in Fig. 2 of the main text and Fig. 6. The subscripts 1, 2, 3, 4, 5 denote the different choices $\Delta t = 0.1, \Delta t = 10, \Delta t = 3000, \Delta t = 4000$ and $\Delta t = 5000$, respectively.

$\Delta\phi/10^{-6}$	1	10	30	50	100	150	200	250	300
$\max \lambda_Z $	3.466×10^{11}	6.610×10^{23}	3.640×10^{37}	1.344×10^{47}	6.555×10^{54}	2.780×10^{63}	9.036×10^{73}	1.292×10^{83}	2.000×10^{93}
$\max \lambda_G $	3.490×10^{11}	6.657×10^{23}	3.666×10^{37}	1.354×10^{47}	6.601×10^{54}	2.799×10^{63}	9.101×10^{73}	1.302×10^{83}	2.014×10^{93}
$\max \lambda_Z $	6.931×10^{11}	1.322×10^{24}	7.281×10^{37}	2.688×10^{47}	1.311×10^{55}	5.559×10^{63}	1.807×10^{73}	2.584×10^{83}	3.999×10^{93}
$\max \lambda_G $	1.536×10^{15}	2.554×10^{28}	1.022×10^{42}	2.675×10^{51}	4.761×10^{58}	4.960×10^{63}	9.174×10^{69}	2.325×10^{75}	1.722×10^{81}
$\max \lambda_Z $	2.699×10^{15}	4.020×10^{28}	1.213×10^{42}	2.223×10^{51}	6.233×10^{57}	1.867×10^{63}	2.588×10^{69}	4.877×10^{75}	6.438×10^{81}
$\max \lambda_G $	4.155×10^{15}	5.345×10^{28}	1.058×10^{42}	9.631×10^{50}	9.668×10^{57}	1.595×10^{62}	4.155×10^{69}	2.112×10^{75}	1.720×10^{81}

(b) The squared correction factors $\max|\lambda_Z|$ and $\max|\lambda_G|$ in Fig. 3 of the main text.

$\beta^{-1} \times 10^{-3}$	1	2	3	4	5	6	7
$\max \lambda_Z $	5010.350	1252.520	557.658	314.530	202.009	140.888	104.035
$\max \lambda_G $	5045.900	1261.410	561.615	316.762	203.442	141.888	104.773
Δt	1	20	40	60	80	100	120
$\max \lambda_Z $	5.000×10^5	5.000×10^5	5.000×10^5	5.000×10^5	5.000×10^5	5.000×10^5	5.000×10^5
$\max \lambda_G $	5.366×10^5	1.866×10^6	4.950×10^6	9.975×10^6	1.699×10^7	2.599×10^7	3.700×10^7

(c) The squared correction factor $\max|\lambda_Z|$ in Figs. 4(a) and (b) of the main text.

$\phi/(\pi/28)$ ($n=0$)	0.5	1.5	2.5	3.5	4.5	5.5	6.5
$\max \lambda_Z $	23.208	23.772	25.061	27.535	32.470	44.639	107.183
$\phi/(\pi/28)$ ($n=1$)	0.5	1.5	2.5	3.5	4.5	5.5	6.5
$\max \lambda_Z $	12430.800	12759.900	13513.000	1457.600	17840.500	24953.000	61525.500
$\phi/(\pi/28)$ ($n=10$)	0.5	1.5	2.5	3.5	4.5	5.5	6.5
$\max \lambda_Z $	4.502×10^{28}	4.620×10^{28}	4.894×10^{28}	5.416×10^{28}	6.460×10^{28}	9.034×10^{28}	2.228×10^{29}
$\phi/(\pi/28)$	7.5	8.5	9.5	10.5	11.5	12.5	13.5
$\max \lambda_Z $	17.807	5.886	3.471	2.414	1.809	1.409	1.119

(d) The squared correction factor $\max|\lambda_Z|$ in Figs. 4(c) and (d) of the main text.

$-\Delta\phi$	-0.052	-0.044	-0.036	-0.029	-0.020	-0.012	-0.004	0.004
$\max \lambda_Z $	5.228×10^{14}	4.638×10^{13}	3.430×10^{12}	2.814×10^{11}	7.196×10^9	1.347×10^8	6.785×10^5	227.077
$-\Delta\phi$	0.006	0.008	0.011	0.012	0.014	0.018	0.022	0.024
$\max \lambda_Z $	135.424	1.026	69.321	81.274	54.709	1.066	34.384	41.311
$-\Delta\phi$	0.027	0.032	0.037	0.040	0.043	0.049	0.056	0.060
$\max \lambda_Z $	28.328	1.002	20.693	24.985	17.674	1.018	13.850	16.673
n	0	1	2	3	4	5	6	7
$\max \lambda_Z $	2026.420	225.154	81.045	41.331	24.978	16.687	11.907	8.894
								6.866
								5.429

the noisy channel. In our experiments, the dephasing rate η (η_1) for the interferometric network with PBSs (BDs) is $\eta = 0.9615$ ($\eta_1 = 0.9995$). As illustrated in Fig. 9, shadows indicate systematic errors which are obtained from the numerical simulation by considering the inaccuracy of wave plates and decoherence in the experiment. We found that the deviation between the experimental data and their theoretical predictions can be explained by the systematic errors.

As we can only implement passive non-unitary operations U with only loss, we need to map them to the desired ones $e^{-iH_{\mathcal{PT}}\tau}$ via a correction factor $\sqrt{\max|\lambda|}$. Thus, for the experimental results of some physical quantities, we also need to correct them by multiplying the correction factor $\sqrt{\max|\lambda|}$.

As shown in Fig. 9, the difference between the experimental data of the magnetization and their theoretical predictions is caused by the imperfection of the experiment. The difference between the experimental data of the two-time correlation function and the partition function and their theoretical predictions is not only related to the imperfection of the experiment, but also related to the squared correction factor $\max|\lambda|$. With the same experimental imperfection, a larger $\max|\lambda|$ magnifies the difference between the experimental data and their theoretical prediction. We show the squared

correction factor $\max |\lambda|$ for each data in Table I.

Appendix F: Correction factors

The correction factor λ is crucial for the precise mapping between H_{eff} and $H_{\mathcal{PT}}$. There are two correction parameters λ_Z and λ_G . The first one λ_Z is the eigenvalue of $e^{-\beta H_{\mathcal{PT}}} e^{-\beta H_{\mathcal{PT}}^\dagger}$. The second one satisfies $\lambda_G = \lambda_{G_1} \lambda_{G_2}$, where λ_{G_1} is the eigenvalue of $e^{-i\Delta t H_{\mathcal{PT}}} e^{i\Delta t H_{\mathcal{PT}}^\dagger}$, and λ_{G_2} is the eigenvalue of $e^{(i\Delta t - \beta) H_{\mathcal{PT}}} e^{(-i\Delta t - \beta) H_{\mathcal{PT}}^\dagger}$. The partition function Z and the measured Z_{eff} are related to each other by $Z = \sqrt{\max |\lambda_Z|} Z_{\text{eff}}$. Similarly, the correction factor $\sqrt{\max |\lambda_G|}$ needs to be multiplied when measuring $\langle \sigma_z(t_2) \sigma_z(t_1) \rangle Z$ to obtain the two-time correlation function $G(t_2, t_1)$. Whereas, neither of the magnetization and the magnetic susceptibility needs to be corrected by the correction factors.

The effect of the correction factors on the measured values of the magnetization, the magnetic susceptibility, the partition function and the two-time correlation function are shown as

$$\begin{aligned} m = \langle \sigma_z \rangle &= \frac{\langle 0 | e^{-\beta H_{\mathcal{PT}}} | 0 \rangle - \langle 1 | e^{-\beta H_{\mathcal{PT}}} | 1 \rangle}{\langle 0 | e^{-\beta H_{\mathcal{PT}}} | 0 \rangle + \langle 1 | e^{-\beta H_{\mathcal{PT}}} | 1 \rangle} \\ &= \frac{\sqrt{\max |\lambda_Z|} \langle 0 | e^{-\beta H_{\text{eff}}} | 0 \rangle - \sqrt{\max |\lambda_Z|} \langle 1 | e^{-\beta H_{\text{eff}}} | 1 \rangle}{\sqrt{\max |\lambda_Z|} \langle 0 | e^{-\beta H_{\text{eff}}} | 0 \rangle + \sqrt{\max |\lambda_Z|} \langle 1 | e^{-\beta H_{\text{eff}}} | 1 \rangle} \\ &= \frac{\langle 0 | e^{-\beta H_{\text{eff}}} | 0 \rangle - \langle 1 | e^{-\beta H_{\text{eff}}} | 1 \rangle}{\langle 0 | e^{-\beta H_{\text{eff}}} | 0 \rangle + \langle 1 | e^{-\beta H_{\text{eff}}} | 1 \rangle} \\ &= m_{\text{eff}}, \end{aligned} \quad (26)$$

$$\chi = \frac{dm}{da} = \frac{m - m'}{\tan \phi - \tan \phi'} = \frac{m_{\text{eff}} - m'_{\text{eff}}}{\tan \phi - \tan \phi'} = \chi_{\text{eff}}, \quad (27)$$

$$\begin{aligned} Z &= \langle 0 | e^{-\beta H_{\mathcal{PT}}} | 0 \rangle + \langle 1 | e^{-\beta H_{\mathcal{PT}}} | 1 \rangle \\ &= \sqrt{\max |\lambda_Z|} \langle 0 | e^{-\beta H_{\text{eff}}} | 0 \rangle + \sqrt{\max |\lambda_Z|} \langle 1 | e^{-\beta H_{\text{eff}}} | 1 \rangle \\ &= \sqrt{\max |\lambda_Z|} (\langle 0 | e^{-\beta H_{\text{eff}}} | 0 \rangle + \langle 1 | e^{-\beta H_{\text{eff}}} | 1 \rangle) \\ &= \sqrt{\max |\lambda_Z|} Z_{\text{eff}}, \end{aligned} \quad (28)$$

and

$$\begin{aligned} G(t_2, t_1) &= \langle \sigma_z(t_2) \sigma_z(t_1) \rangle - \langle \sigma_z(t_2) \rangle \langle \sigma_z(t_1) \rangle \\ &= \frac{1}{Z} (\langle \sigma_z(t_2) \sigma_z(t_1) \rangle Z) - m^2 \\ &= \frac{\sqrt{\max |\lambda_G|} (\langle \sigma_z(t_2) \sigma_z(t_1) \rangle Z)_{\text{eff}}}{\sqrt{\max |\lambda_Z|} Z_{\text{eff}}} - m_{\text{eff}}^2, \end{aligned} \quad (29)$$

where

$$\begin{aligned} (\langle \sigma_z(t_2) \sigma_z(t_1) \rangle Z)_{\text{eff}} &= \langle 0 | e^{-i\Delta t H_{\text{eff}}} | 0 \rangle \langle 0 | e^{(i\Delta t - \beta) H_{\text{eff}}} | 0 \rangle \\ &\quad - \langle 0 | e^{-i\Delta t H_{\text{eff}}} | 1 \rangle \langle 1 | e^{(i\Delta t - \beta) H_{\text{eff}}} | 0 \rangle \\ &\quad - \langle 1 | e^{-i\Delta t H_{\text{eff}}} | 0 \rangle \langle 0 | e^{(i\Delta t - \beta) H_{\text{eff}}} | 1 \rangle \\ &\quad + \langle 1 | e^{-i\Delta t H_{\text{eff}}} | 1 \rangle \langle 1 | e^{(i\Delta t - \beta) H_{\text{eff}}} | 1 \rangle. \end{aligned} \quad (30)$$

Thus, the correction factor λ only affects the partition function and two-time correlation function, but has no effect on the magnetization and the magnetic susceptibility. We note that the huge correction factor in Tables I(a) and (b) is mostly cancelled in forming the ratio between $\sqrt{\max |\lambda_G|}$ and $\sqrt{\max |\lambda_Z|}$ in Eq. (29).

Appendix G: Comparison with previous works

We compare the experimental results of the Yang-Lee zeros and edge singularity phenomena in this work with other previous experimental works as illustrated in Table II. We emphasize that our work is the first to measure all the critical exponents of the magnetization, magnetic susceptibility, two-time correlation function, and the density of zeros about the Yang-Lee edge singularity. Measurements of the entire set of critical exponents provide the key to the determination of the universality class of the underlying physics. Specifically, Ref. [29] estimates the dependence on the imaginary magnetic field via mathematical analytic continuation from measurements results for the real magnetic field. This reference measured the critical exponent of the density distribution of Yang-Lee zeros but did not measure other critical exponents. References [28, 31, 32, 35] only measured the locations of Yang-Lee zeros but did not measure critical exponents.

In contrast, our work directly controls the pure imaginary magnetic field via photon loss, and has the distinct advantages in the sense that we can directly measure the partition function, Yang-Lee zeros, and the physical quantities under the imaginary magnetic field. In particular, two-time correlation functions can only be measured by our method. This is a consequence of the fact that our method has the decisive ability to perform real-time simulations under the imaginary magnetic field by using open systems.

We also stress that the temperature dependence of the Yang-Lee critical phenomenon can only be measured by our method. In this sense, our work experimentally realizes the Yang-Lee quantum criticality beyond the classical regime.

TABLE II. Comparison of Yang-Lee zeros and edge singularity phenomena observed in this work with other previous experimental works.

Ref.	Yang-Lee zeros	Critical exponents			
		magnetization	susceptibility	correlation functions	the density distribution of zeros
[29]	yes	no	no	no	yes
[31]	yes	no	no	no	no
[32]	yes	no	no	no	no
[28]	yes	no	no	no	no
[35]	yes	no	no	no	no
our work	yes	yes	yes	yes	yes

This work is supported by the National Natural Science Foundation of China (Grant Nos. 92265209 and 12025401). MU acknowledges support by KAKENHI Grant No. JP22H01152 from the Japan Society for the Promotion of Science and by the CREST program ‘‘Quantum Frontiers’’ (Grant No. JPMJCR23I1) by the Japan Science and Technology Agency. MN is supported by KAKENHI Grant No. JP20K14383 from the

Japan Society for the Promotion of Science. NM is supported by KAKENHI Grant No. JP21J11280 from the Japan Society for the Promotion of Science. HQL acknowledges support from the National Natural Science Foundation of China (Grant No. 12088101).

* ueda@cat.phys.s.u-tokyo.ac.jp

† gnep.eux@gmail.com

- [1] C. N. Yang and T. D. Lee, Statistical theory of equations of state and phase transitions. I. Theory of condensation, *Phys. Rev.* **87**, 404 (1952).
- [2] T. D. Lee and C. N. Yang, Statistical theory of equations of state and phase transitions. II. Lattice gas and Ising model, *Phys. Rev.* **87**, 410 (1952).
- [3] M. E. Fisher, Yang-Lee edge singularity and ϕ^3 field theory, *Phys. Rev. Lett.* **40**, 1610 (1978).
- [4] B. Simon and R. B. Griffiths, The $(\varphi^4)_2$ field theory as a classical Ising model, *Communications in Mathematical Physics* **33**, 145 (1973).
- [5] C. M. Newman, Zeros of the partition function for generalized Ising systems, *Communications on Pure and Applied Mathematics* **27**, 143 (1974).
- [6] E. H. Lieb and A. D. Sokal, A general Lee-Yang theorem for one-component and multicomponent ferromagnets, *Communications in Mathematical Physics* **80**, 153 (1981).
- [7] P. J. Kortman and R. B. Griffiths, Density of zeros on the Lee-Yang circle for two Ising ferromagnets, *Phys. Rev. Lett.* **27**, 1439 (1971).
- [8] D. A. Kurtze and M. E. Fisher, Yang-Lee edge singularities at high temperatures, *Phys. Rev. B* **20**, 2785 (1979).
- [9] M. E. Fisher, Yang-Lee edge behavior in one-dimensional systems, *Prog. Theor. Phys. Suppl.* **69**, 14 (1980).
- [10] J. L. Cardy, Conformal invariance and the Yang-Lee edge singularity in two dimensions, *Phys. Rev. Lett.* **54**, 1354 (1985).
- [11] J. L. Cardy and G. Mussardo, S-matrix of the Yang-Lee edge singularity in two dimensions, *Phys. Lett. B* **225**, 275 (1989).
- [12] A. B. Zamolodchikov, Two-point correlation function in scaling Lee-Yang model, *Nucl. Phys. B* **348**, 619 (1991).
- [13] T. Sumaryada and A. Volya, Thermodynamics of pairing in mesoscopic systems, *Phys. Rev. C* **76**, 024319 (2007).
- [14] T. Kist, J. L. Lado, and C. Flindt, Lee-Yang theory of criticality in interacting quantum many-body systems, *Phys. Rev. Res.* **3**, 033206 (2021).
- [15] P. M. Vecsei, J. L. Lado, and C. Flindt, Lee-Yang theory of the two-dimensional quantum Ising model, *Phys. Rev. B* **106**, 054402 (2022).
- [16] Kh. P. Gnatenko, A. Kargol, and V. M. Tkachuk, Two-time correlation functions and the Lee-Yang zeros for an interacting Bose gas, *Phys. Rev. E* **96**, 032116 (2017).
- [17] R. Couvreur, J. L. Jacobsen, and H. Saleur, Entanglement in nonunitary quantum critical spin chains, *Phys. Rev. Lett.* **119**, 040601 (2017).
- [18] P.-Y. Chang, J.-S. You, X. Wen, and S. Ryu, Entanglement spectrum and entropy in topological non-Hermitian systems and nonunitary conformal field theory, *Phys. Rev. Res.* **2**, 033069 (2020).
- [19] C. Itzykson and J.-B. Zuber, Two-dimensional conformal invariant theories on a torus, *Nucl. Phys. B* **275**, 580 (1986).
- [20] C. Itzykson, H. Saleur, and J.-B. Zuber, Conformal invariance of nonunitary 2d-models, *Europhys. Lett.* **2**, 91 (1986).
- [21] A. Deger and C. Flindt, Determination of universal critical exponents using Lee-Yang theory, *Phys. Rev. Res.* **1**, 023004 (2019).
- [22] A. Deger, F. Brange, and C. Flindt, Lee-Yang theory, high cumulants, and large-deviation statistics of the magnetization in the Ising model, *Phys. Rev. B* **102**, 174418 (2020).
- [23] S. Peotta, F. Brange, A. Deger, T. Ojanen, and C. Flindt, Determination of dynamical quantum phase transitions in strongly correlated many-body systems using Loschmidt cumulants, *Phys. Rev. X* **11**, 041018 (2021).
- [24] M. Heyl, Dynamical quantum phase transitions: A review, *Rep. Prog. Phys.* **81**, 054001 (2018).
- [25] A. Connelly, G. Johnson, F. Rennecke, and V. V. Skokov, Universal location of the Yang-Lee edge singularity in $O(N)$ theories, *Phys. Rev. Lett.* **125**, 191602 (2020).
- [26] S. J. Jian, Z. C. Yang, Z. Bi, and X. Chen, Yang-Lee edge singularity triggered entanglement transition, *Phys. Rev. B* **104**, L161107 (2021).
- [27] P. Jurcevic, H. Shen, P. Hauke, C. Maier, T. Brydges, C. Hempel, B. P. Lanyon, M. Heyl, R. Blatt, and C. F. Roos, Direct observation of dynamical quantum phase transitions in an interacting many-body system, *Phys. Rev. Lett.* **119**, 080501 (2017).
- [28] N. Fläschner, D. Vogel, M. Tarnowski, B. S. Rem, D.-S. Lühmann, M. Heyl, J. C. Budich, L. Mathey, K. Sengstock, and C. Weitenberg, Observation of dynamical vortices after quenches in a system with topology, *Nat. Phys.* **14**, 265 (2018).
- [29] C. Binek, W. Kleemann, and H. A. Katori, Yang-Lee edge singularities determined from experimental high-field magnetization data, *J. Phys.: Condens. Matter* **13**, L811 (2001).
- [30] B. B. Wei and R. B. Liu, Lee-Yang zeros and critical times in decoherence of a probe spin coupled to a bath, *Phys. Rev. Lett.* **109**, 185701 (2012).
- [31] X. Peng, H. Zhou, B. B. Wei, J. Cui, J. Du, and R. B. Liu, Experimental observation of Lee-Yang zeros, *Phys. Rev. Lett.* **114**, 010601 (2015).
- [32] K. Brandner, V. F. Maisi, J. P. Pekola, J. P. Garrahan, and C. Flindt, Experimental determination of dynamical Lee-Yang zeros, *Phys. Rev. Lett.* **118**, 180601 (2017).
- [33] B. B. Wei, Probing Yang-Lee edge singularity by central spin decoherence, *New J. Phys.* **19**, 083009 (2017).
- [34] B. B. Wei, Probing conformal invariant of non-unitary two dimensional systems by central spin decoherence, *Sci. Rep.* **8**, 3080 (2018).
- [35] A. Francis, D. Zhu, C. Huerta Alderete, S. Johri, X. Xiao, J. K. Freericks, C. Monroe, N. M. Linke, and A. F. Kemper, Many-body thermodynamics on quantum computers via partition function zeros, *Sci. Adv.* **7**, eabf2447 (2021).
- [36] M. Suzuki, Relationship between d-dimensional quantum spin systems and (d+1)-dimensional Ising systems: Equivalence, critical exponents and systematic approximants of the partition function and spin correlations, *Prog. Theor. Phys.* **56**, 1454 (1976).
- [37] J. B. Kogut, An introduction to lattice gauge theory and spin systems, *Rev. Mod. Phys.* **51**, 659 (1979).
- [38] N. Matsumoto, M. Nakagawa, and M. Ueda, Embedding the Yang-Lee quantum criticality in open quantum systems, *Phys. Rev. Res.* **4**, 033250 (2022).
- [39] See the Supplemental Material for more details.
- [40] C. M. Bender and S. Boettcher, Real spectra in non-Hermitian Hamiltonians having PT Symmetry, *Phys.*

- Rev. Lett. **80**, 5243 (1998).
- [41] C. M. Bender, D. C. Brody, and H. F. Jones, Complex extension of quantum mechanics, Phys. Rev. Lett. **89**, 270401 (2002).
- [42] M. V. Berry, Physics of nonhermitian degeneracies, Czech. J. Phys. **54**, 1039 (2004).
- [43] W. D. Heiss, The physics of exceptional points, J. Phys. A: Math. Theor. **45**, 444016 (2012).
- [44] K. Uzelac, P. Pfeuty, and R. Jullien, Yang-Lee Edge Singularity from a Real-Space Renormalization-Group Method, Phys. Rev. Lett. **43**, 805 (1979).
- [45] G. Von Gehlen, Critical and off-critical conformal analysis of the Ising quantum chain in an imaginary field, J. Phys. A: Math. Gen. **24**, 5371 (1991).
- [46] S. Yin, G.-Y. Huang, C.-Y. Lo, and P. Chen, Kibble-Zurek scaling in the Yang-Lee edge singularity, Phys. Rev. Lett. **118**, 065701 (2017).
- [47] L. J. Zhai, G.-Y. Huang, and H.-Y. Wang, Pseudo-Yang-Lee edge singularity critical behavior in a non-Hermitian Ising model, Entropy **22**, 780 (2020).
- [48] P. R. Halmos, Normal dilations and extensions of operators, Summ. Bras. Math. **2**, 125 (1950).
- [49] C. Sparrow, E. Martin-Lopez, N. Maraviglia, A. Neville, C. Harrold, J. Carolan, Y. N. Joglekar, T. Hashimoto, N. Matsuda, J. L. O'Brien, D. P. Tew, and A. Laing, Simulating the vibrational quantum dynamics of molecules using photonics, Nature (London) **557**, 660 (2018).
- [50] L. Xiao, K. K. Wang, X. Zhan, Z. H. Bian, K. Kawabata, M. Ueda, W. Yi, and P. Xue, Observation of critical phenomena in parity-time-symmetric quantum dynamics, Phys. Rev. Lett. **123**, 230401 (2019).
- [51] L. Xiao, K. K. Wang, X. Zhan, Z. H. Bian, K. Kawabata, M. Ueda, W. Yi, and P. Xue, Observation of critical phenomena in parity-time-symmetric quantum dynamics, Phys. Rev. Lett. **123**, 230401 (2019).
- [52] L. Xiao, T. S. Deng, K. K. Wang, G. Y. Zhu, Z. Wang, W. Yi, and P. Xue, Non-Hermitian bulk-boundary correspondence in quantum dynamics, Nat. Phys. **16**, 761-766 (2020).
- [53] K. K. Wang, L. Xiao, J. C. Budich, W. Yi, and P. Xue, Simulating exceptional non-Hermitian metals with single-photon interferometry, Phys. Rev. Lett. **127**, 026404 (2021).